

Full Paper

Evaluation of Thin Film Titanium Nitride Electrodes for Electroanalytical Applications

Carolina Nunes Kirchner,^a Karl Heinz Hallmeier,^b Rüdiger Szargan,^b Thomas Raschke,^c Christian Radehaus,^c Gunther Wittstock,^{a,*}

^a Carl von Ossietzky University Oldenburg, Faculty of Mathematics and Natural Sciences, Center of Interface Science (CIS), Department of Pure and Applied Chemistry and Institute of Chemistry and Biology of the Marine Environment, D-26111 Oldenburg, Germany

*e-mail: gunther.wittstock@uni-oldenburg.de

^b University of Leipzig, Wilhelm Ostwald Institute of Physical and Theoretical Chemistry, Linnéstrasse 2, D-04103 Leipzig, Germany

^c Chemnitz University of Technology, Department of Electrical Engineering and Information Technology, D-09107 Chemnitz, Germany

Received: January 24, 2007

Accepted: February 22, 2007

Abstract

Titanium nitride is a hard and inert conducting material that has yet not been widely used as electrode material for electroanalytical applications although there are highly developed protocols available to produce well adherent micro and nanostructured electrodes. In this paper the possibilities of using titanium nitride thin films for electroanalytical applications is investigated. Scanning electrochemical microscope (SECM) was used for analysis of the redox kinetics of a selected fast redox couple at thin films of titanium nitride (TiN) in different thicknesses. The investigation was carried out by approaching an amperometric ultramicroelectrode (UME) to the TiN film while the soluble redox couple (ferrocenemethanol/ferrociniummethanol) served as mediator in a SECM configuration. The substrate was biased at a potential so that it rereduces the species being produced at the UME, thus controlling the feedback effect. Normalized current–distance curves were fitted to the theoretical model in order to find the apparent heterogeneous standard rate constant (k°) at the sample. The data are further supported by structural investigation of the TiN films using scanning force microscopy and X-ray photoelectron spectroscopy. It was found that the kinetics are little influenced by prolonged storage in air. The heterogeneous standard rate constants in 2 mM ferrocenemethanol were $(0.73 \pm 0.05) \times 10^{-3} \text{ cm s}^{-1}$ for 20 nm TiN thin layer, $(1.5 \pm 0.2) \times 10^{-3} \text{ cm s}^{-1}$ for 100 nm TiN thin layer and $(1.3 \pm 0.2) \times 10^{-3} \text{ cm s}^{-1}$ for 300 nm TiN thin layer after prolonged storage in air. Oxidative surface treatment (in order to remove organic adsorbates) decreased the kinetics in agreement with a thicker oxide layer on the material. The results suggest that their direct use for amperometric detection of reversible redox systems in particular at miniaturized configurations may be advantageous.

Keywords: Scanning electrochemical microscopy (SECM), Feedback mode, Approach curves, Titanium nitride, Standard rate constant, X-ray photoelectron spectroscopy (XPS)

DOI: 10.1002/elan.200703832

Dedicated to Professor Dr. Dr. h.c. Lothar Beyer (Leipzig) on the Occasion of His 70th Birthday

1. Introduction

Titanium nitride films exhibits an exceptional combination of chemical, physical, mechanical and electrical properties, such as a high degree of hardness, chemical stability, high thermal conductivity, an immunity to wear and corrosion, chemical inertness, biocompatibility, and resistance to atomic diffusion within its matrix [1–4]. Thin films of TiN can be deposited by a number of physical and chemical vapor deposition methods including evaporation, ion plating and sputtering [2, 5–7]. The growth of TiN was studied [8] and showed that it forms a sodium chloride lattice already at very small sizes of TiN clusters. The properties of thin films, like preferred orientation of lattice plane and

electrical resistance, grown by physical and chemical vapor deposition methods are highly dependent on total gas pressure, partial pressures of reactive gases, deposition rate, temperature and substrate material [9–15], which makes it suitable for a wide range of applications if the material properties are tuned right. Consequently, patterned TiN is a candidate material for microelectrode arrays [2]. Several studies about structural, mechanical and electrical properties of TiN thin films have been completed in the last years [1–7, 9–19]. They also include studies about the oxidation kinetics of TiN [20–22]. Titanium nitride has been used as the sensitive material in all solid-state potentiometric pH electrode [23]. The electrochemical inactivation of adherently growing bacteria on TiN electrodes in seawater was

demonstrated using a potentiostatic treatment that takes advantage of inertness of TiN [24]. On the other hand TiN is considered as a biocompatible material [2, 25] and has been used for electrically contacting adherent cells and tissue [26].

One particular attractive feature of TiN thin film electrodes are the highly developed protocols that allow to produce well adherent micro- or nanostructured electrodes. Detection schemes that rely on redox-cycling at interdigitated electrode arrays (IDAs) show an increasing sensitivity with decreasing band size and electrode–electrode distances [27, 28]. Remarkable effects can be expected if electrode and gap sizes are pushed well below 1 μm . However, up to now there is no well-developed technology for the mass production of nanometer-sized IDAs with noble metal electrodes. Developing such a technology is not an easy task because of the inertness of the noble metals typically employed for analytical electrodes. Wet etching steps are problematic because they would likely destroy the etch mask. Dry etching procedures are problematic because there are no suitable gaseous etching products, e.g., AuX_n that are able to transport away the etched noble metal. Few reports describe reactive ion etching of gold [29–31] (a dry process), but the described structures are larger than 500 nm. Reference [32] describes Au structures with sub-100 nm resolution obtained by negative nanoimprint lithography. However, a wet etching step with its limitations was used during the preparation. Lift-off techniques require thick mask layers in order to remove them after deposition contradicting the requirement for small distances. Ion milling as another alternative would distribute the material over the whole surrounding area and is not well suited for mass production. On the other side there is a well-developed and established TiN deposition and structuring technology for the mass production by the microelectronic industry [33]. This technology can be scaled down to nanostructures and it would be possible to produce nanosized IDAs even in mass production. For electroanalytical purposes some groups demonstrated the galvanic deposition of Pt on top of TiN structures in order to improve the electroanalytical characteristics of TiN electrodes [34] or to use TiN as catalytically inactive back contact for combinatorial libraries of Pt-Ru electrocatalysts for fuel cell anodes [17].

In this work we evaluate the properties of thin film TiN electrodes for electroanalytical application. Double layer charging current densities and the heterogeneous electron transfer kinetics for the ferrocenemethanol (Fc)/ferrociummethanol (Fc^+) couple were investigated using scanning electrochemical microscopy (SECM). The data are correlated to structural characterization by scanning force microscopy (SFM) and X-ray photoelectron (XP) spectroscopy.

2. Experimental

2.1. Solutions and Chemicals

All chemicals were reagent grade and were used as received. All solutions were prepared with deionized water. Ferrocenemethanol (Fc, ABCR GmbH & Co. KG, Karlsruhe, Germany) was dissolved in ethanol and diluted in 0.1 M sodium sulfate (Carl Roth GmbH & Co, Karlsruhe, Germany).

For the study of the potential window in acidic, neutral and alkaline solution the following chemicals were used: 0.1 M NaOH (Carl Roth GmbH & Co, Karlsruhe, Germany), 0.1 M phosphate buffer ($\text{NaHPO}_4 \cdot \text{H}_2\text{O}$, Scharlau Chemie S. A., Barcelona, Spain; $\text{NaH}_2\text{PO}_4 \cdot 2\text{H}_2\text{O}$, Fluka Chemie GmbH, Buchs, Switzerland) and 0.05 M H_2SO_4 (Merck KGaA, Darmstadt, Germany).

TiN layers were deposited on boron-doped p-Si(100) substrates with a resistivity of 12–20 Ω cm. The substrates were cleaned and 100 nm thermal oxide was grown on them. TiN was applied by reactively sputtering Ti in a gas atmosphere consisting of Ar and N_2 at a total pressure of 0.2 Pa using a DC magnetron system (HZSÜ-03, Hochvakuum Dresden, Germany) at 2 kW. The gas atmosphere was formed by adjusting the gas volume fluxes F_{N_2} and F_{Ar} to $F_{\text{N}_2}/(F_{\text{N}_2} + F_{\text{Ar}}) = 0.2$. The sputter rate was 0.47 nm s^{-1} . The atomic ratio is influenced by the composition of the gas atmosphere and by the transmitted power at the sample. The N/Ti atomic ratio in the sample was 1.01 as determined by Rutherford backscattering spectroscopy and elastic backscattering detection. In addition depth profiles were recorded by Auger electron spectroscopy. The layers had thicknesses of 20 nm, 100 nm and 300 nm. An extensive account of the preparation and analysis is available [35].

The TiN electrodes were stored for prolonged time in air (1 month to 5 years). They were washed in ethanol, deionized water and then dried with Ar gas before the measurements. The reported data here are for electrodes aged 5 years (native samples). Results for electrodes tested after 1 month and 3 years were identical. One sample set was cleaned by a 5 min treatment with UV light (UV tip cleaner, Bioforce Nanoscience, Ames, Iowa, USA) that causes the generation of ozone (UV/ozone-treated samples). Contact to TiN was made with silver epoxy joint to copper wires.

2.2. Instrumentation

A home-build SECM instrument was used to record the approach curves. The SECM setup consists of a stepper motor positioning system (Märzhäuser GmbH & Co KG, Wetzlar, Germany) with a step increment of 50 nm. The positioning system moves the UME in three orthogonal directions relative to the sample surface. In the x and y direction (horizontal to the sample) it operates in closed-loop mode, and in the z direction (vertical to the sample) it operates in open loop mode. SECM data were acquired

through an ADC board (PCI-DAS 1602/16, Plug-in Electronic GmbH, Eichenau, Germany) with 16 bit resolution. The analog inputs were connected to the analog output ports of a bipotentiostat (CHI 700B, CH Instruments, Austin, TX, USA) that controlled the potential of the UME (working electrode 1) and the TiN thin film (working electrode 2) with respect to a reference electrode (Ag|AgCl|3 M KCl) to which all potentials are referred to. A Pt auxiliary electrode completed the four electrode cell.

The motor position and data acquisition are controlled by a homemade SECM program written in C++ language. SECM control software separates the main application block (experiment control; data acquisition and visualization) and the hardware access, therefore becoming virtually independent on particular hardware (although it provides instrument-specific tools for the hardware setup). The hardware access is realized in form of hardware-specific dynamic link libraries (DLL).

Cyclic voltammograms (CV) were measured using a three-electrode arrangement and CHI 700B and CHI 660A potentiostats (CH Instruments, Austin, TX, USA) with Pt auxiliary electrode and Ag|AgCl|3 M KCl reference electrode.

Topography and roughness of the TiN films were obtained by SFM in the Tapping Mode with a Veeco Dimension 3100 stage and a Nanoscope IIIA controller (Veeco Instruments Inc., Santa Barbara, CA, USA).

XP spectra of Ti, N, C and O were obtained with an ESCALAB 220 iXL (VG, East Grinstead, UK) with a hemispherical analyzer at a pressure $< 5 \times 10^{-8}$ Pa using monochromatized Al K α radiation for excitation. A pass energy of 50 eV and 10 eV was used for survey scans and individual lines. The binding energy (BE) scale of the spectrometer was calibrated by Au 4f_{1/2} (84.0 eV), Ag 3d_{5/2} (368.3 eV) and Cu 2p_{3/2} (932.7 eV). The BE energy scales showed no charging effects, giving in the case of the untreated sample a value of 284.6 eV for the main C 1s component (sp² carbon – graphite-like) and 285 eV for the spectrum of the sputtered samples (sp³ carbon – the well known aliphatic contamination). Spectra were recorded immediately after introduction into the ultra high vacuum and after sputtering 5 min with Ar⁺ ion of 3 keV kinetic energy. The spectra were decomposed into individual contributions using the program UNIFIT 2006 [36]. The graphs show in the upper parts the measured spectrum and the baseline, the lower sections show the fitted components and their sum.

2.3. Procedures

All SECM experiments were carried out with a 25 μ m diameter Pt UME fabricated according to [37]. 25 μ m diameter Pt wire (Goodfellow, Cambridge, U. K.) was sealed into a 5 cm Pyrex glass capillary under vacuum. The UME was polished and shaped conically by a wheel with 180 grid paper disks (Leco, St. Joseph, MI, USA) and micro-polishing cloth with 1.0 μ m, 0.3 μ m, and 0.05 μ m alumina

(Buehler, Lake Bluff, IL, USA). The UME was sharpened to $RG \approx 10$, where RG is the ratio between the diameters of the glass sheath r_g and the active electrode radius r_T . Before each experiment, the UME was polished with 0.3 and 0.05 μ m alumina powder and rinsed with water.

The approach curves were obtained by moving the UME toward the TiN surface and recording the amperometric UME current i_T as a function of the distance d between sample and UME. Fc was oxidized at the UME at a potential $E_T = 0.4$ V under diffusion-controlled conditions. The generated Fc⁺ diffused towards the substrates (TiN, or glass as reference). The externally biased TiN substrate reduced Fc⁺ to Fc. The recycling of the Fc at the TiN was controlled by adjusting substrate potentials E_S . Initially, an approach curve was recorded towards a smooth glass surface until the mechanical contact between the glass sheath of the UME and the sample surface was detected as a suddenly established constant current. From this approach curve the distance between the UME active area and the sample in the moment of the mechanical touch of the insulating sheath with the sample was determined. Afterwards, the glass sample was exchanged against the TiN sample without changing the mounting of the UME. After detecting the mechanical touch between UME sheath and the TiN sample in the same way as on the glass electrode, the zero distance point could be established for the samples with finite kinetics. The approach curves were recorded at three Fc concentrations (1.0, 2.0, 3.0 mM).

3. Results and Discussion

3.1. Structural Characterization

3.1.1. Scanning Force Microscopy (SFM)

Topography and roughness were examined for the different layers by scanning force microscopy. Figure 1a shows a representative SFM image of the 300 nm thick TiN layer. The roughness is given as the root mean square (RMS) value determined on an area of 5 by 5 μ m². It showed a linear dependency on thickness (Fig. 1b).

3.1.2. X-Ray Photoelectron Spectroscopy

Signals for Ti, N, O and C were found in XP spectra and were analyzed in more detail. On native samples the high-resolution Ti 2p signal shows three components (Fig. 2a). Because the Ti 2p_{1/2} signal is superimposed with a complicated background including also a possible energy-loss structure, attention should be directed only on the Ti 2p_{3/2} signal at binding energies (BE) of 454–460 eV. The three components can be assigned to TiN (455.1 eV [38]), titanium oxonitride (456.3 eV) and TiO₂ (458.1 eV). This pattern is typical for TiN layers prepared in this way [23–25]. However, the relative intensities of the components are highly dependent on the preparation condition. Interestingly, the bulk TiN material has the lowest Ti-N contribution

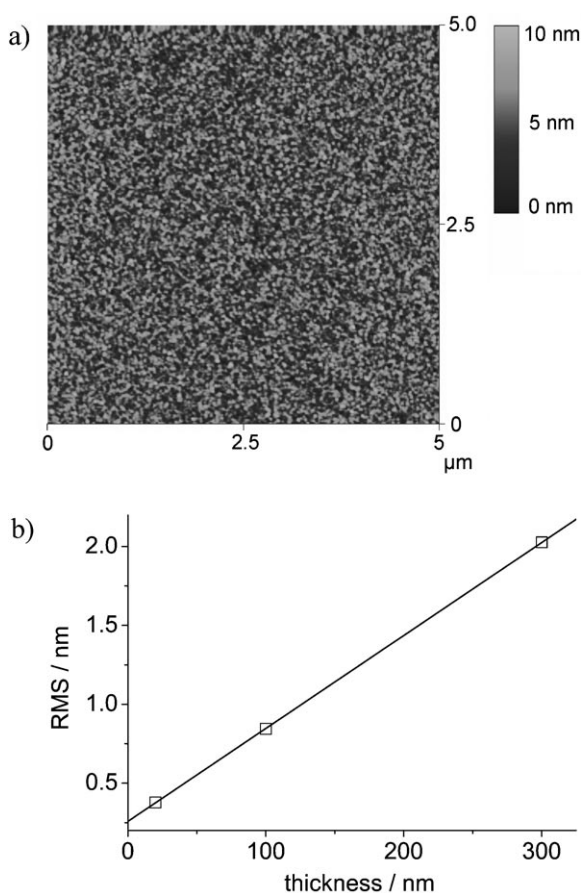


Fig. 1. Scanning force microscopy of TiN layer, a) image of a 300 nm thick layer; b) RMS values determined on an $5 \times 5 \mu\text{m}^2$ area on different TiN samples as a function of layer thickness.

at the surface layer. Therefore, also the energy loss structure associated with Ti^{3+} centers and expected at 455.7 eV [39, 40] has a lower importance for this sample.

The main component of the N 1s spectra at 397.3 eV (Fig. 2c) agrees very well with literature references for the nitride [38, 40]. In addition, there is a higher energy contribution that may result from nitrogen-oxygen compounds at the surface. The origin of two low-energy component at 395.8 eV and 396.5 eV is presently unclear. The BE values are unusually low for N 1s signals.

The O 1s spectra (Fig. 2d) is formed by a contribution of oxidic oxygen atoms (529.6 eV) and an hydroxydic component at 531.4 eV due to OH^- groups from the humidity during the sample treatment in air. The C 1s spectra (Fig. 2b) has a main component of sp^2 -hybridized carbon at 286.4 eV. The BE corresponds to that of graphite, but this assignment has not been further verified. Carbides were not detected. Two components at higher BE are typical for organic contaminations that must be expected after prolonged storage in air (286.0 eV, 288.2 eV).

The assignments are supported by a moderate sputtering of the sample by 5 min Ar^+ bombardment intended to remove the topmost contamination layer (Fig. 3). The total

amount of carbon was drastically reduced. The main component is now located at 285.0 eV – a value expected for sp^3 -hybridized carbon not connected to electronegative elements (Figure 3b). The N 1s component at 395.8 eV was completely removed (Fig. 3c). This suggests that this unknown component is present only at the very surface of the sample and probably results from a contamination. The total amount of oxygen was decreased, whereby in particular the oxygen bound in organic contaminants (531.4 eV) were reduced (Fig. 3d). In the Ti $2p_{3/2}$ spectra the intensity of the bulk component at 455.0 eV has a much higher intensity and the associated energy-loss structure at 455.7 eV had to be considered in the spectral analysis (Fig. 3a).

The UV/ozone treatment of the samples leads to a partial removal of the carbon contamination and an almost negligible increase in the TiO_2 and oxidic oxygen component.

3.2. Electrical and Basic Electrochemical Characteristics

3.2.1. Four Point Resistance Measurement

The resistivity of the TiN layers were measured using the four-point resistance measurement and were calculated $122.3 \mu\Omega \text{ cm}$, $90.1 \mu\Omega \text{ cm}$ and $119.9 \mu\Omega \text{ cm}$ for 20 nm 100 nm and 300 nm TiN respectively. The values are in agreement with literature [15].

3.2.2. Double Layer Charging Currents and Potential Window

Figure 4 illustrates the potential window of TiN thin-film electrodes in acidic (Fig. 4, curve 1), in neutral (Fig. 4, curve 2) alkaline solutions (Fig. 4, curve 3). The potential windows were also tested as a function of the TiN layer thickness. The potential range useful for electroanalytical applications is limited by proton reduction at the negative side and formation of passive films at the positive side. The values quoted in Table 1 were taken as those values when the magnitude of the capacitive current observed between 0 and +0.3 V changed by more than 30%. The negative limits were taken from a cyclic voltammograms starting from 0 V in negative direction. Since the current rises gradually, there is some variation in the exact potential when the criteria is met. After the negative limit was established, the positive limit was tested by successively increasing the positive potential limit. The values in Table 1 varied only slightly with the tendency that the useful potential window increased with the TiN layer thickness (Table 1). The upper limits of the potential range compare well to the useful potential range of noble metal electrodes such a gold. The voltammograms of Figure 4 were recorded afterwards to include the onsets of proton reduction and the formation of a passive film for an illustrative overview.

While TiN electrodes used for pacemaker electrodes were optimized with the aim of obtaining a large surface area, a large charging current caused by an internal surface would

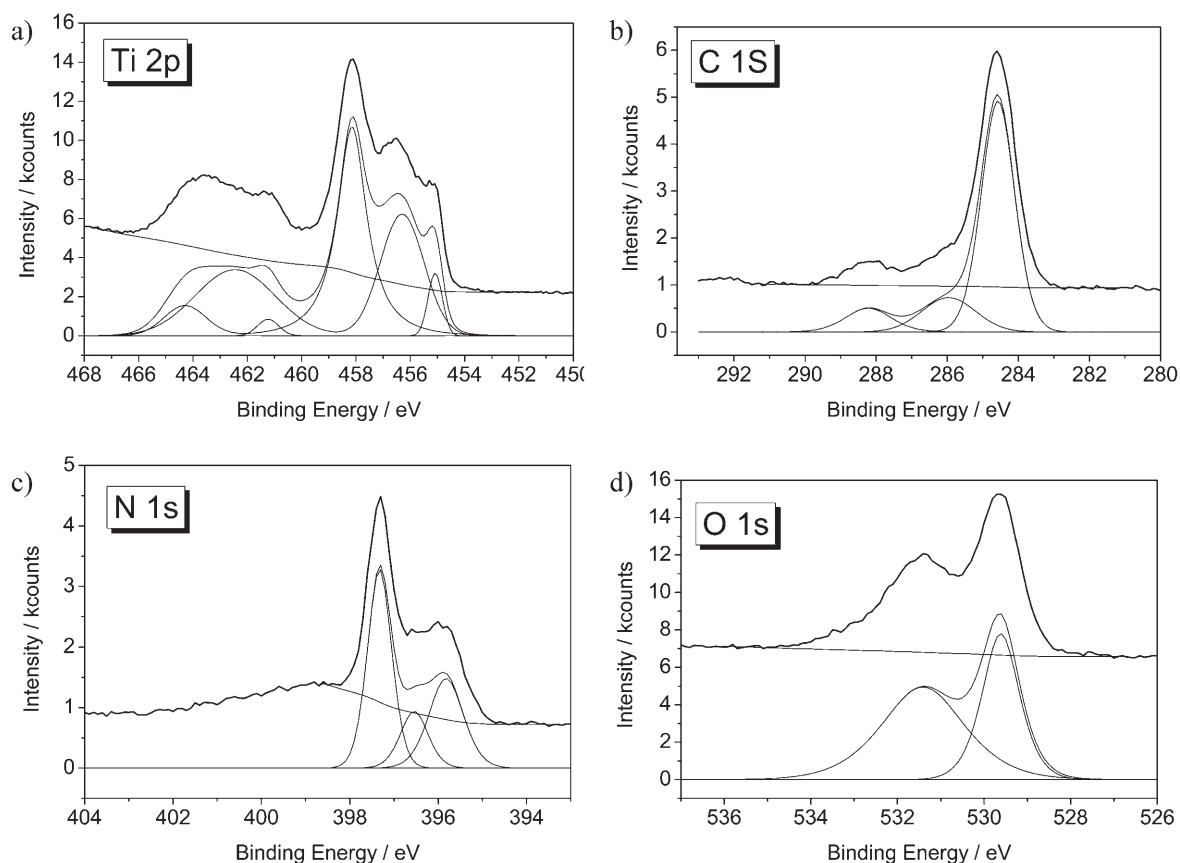


Fig. 2. XPS spectra of native TiN layers after prolonged storage in air. a) Ti 2p, b) C 1s, c) N 1s, d) O 1s.

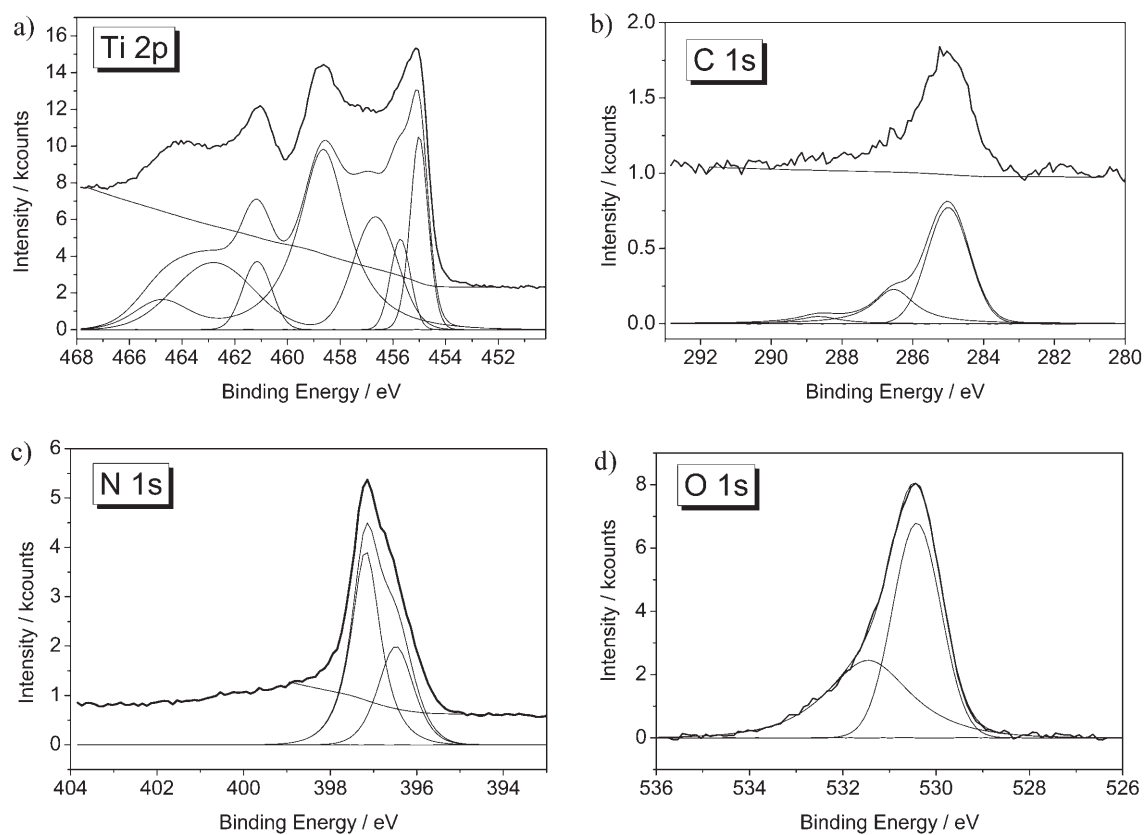


Fig. 3. XPS spectra of native TiN layers after 5 min Ar^+ sputtering. a) Ti 2p, b) C 1s, c) N 1s, d) O 1s.

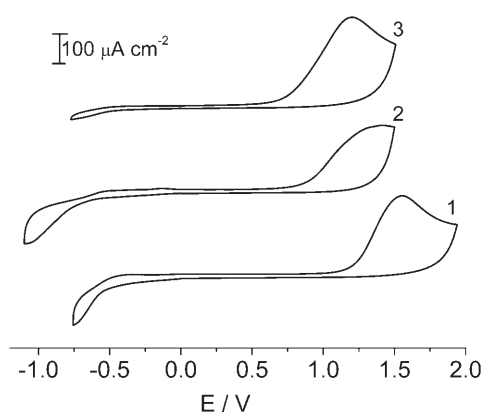


Fig. 4. Comparison of the useful potential ranges for a 100 nm TiN electrode in 1) 0.05 M H_2SO_4 , 2) 0.1 M phosphate buffer, and 3) 0.1 M NaOH.

be undesirable for electroanalytical application as it contributes to the background signal. The charging current densities at TiN investigated depend on the TiN thickness and are 3–8 times larger than that on gold electrodes of the same geometric area (Fig. 5). Most likely, the signal at TiN is also influenced by pseudocapacitances. They result from the electrochemical conversion of surface-bound functional groups. However, it seems that these contributions can be kept under control.

Figure 6 compares the CVs of ferrocenemethanol at TiN and at gold. At the gold electrode the difference of the peak potentials is close to the value of 59 mV expected for a reversible one-electron couple. The response at the TiN shows a larger peak separation of 105 mV. Assuming the equality of the diffusion coefficients for the oxidized and reduced form and taking the experimentally determined diffusion coefficient for ferrocenemethanol of $6 \times 10^{-6} \text{ cm}^2 \text{ s}^{-1}$, a heterogeneous rate constant of $3.0 \times 10^{-3} \text{ cm s}^{-1}$ can be estimated [41]. The low value for the usually fast redox couple results from the internal resistance of the TiN layers and/or slow electron transfer kinetics at the TiN surface. In view of the low resistance obtained from the four-point resistance measurements it seems that the heterogeneous electron transfer kinetics has the dominating influence. Despite this effect, the CV is well developed and for a number of electroanalytical applications such a response might be sufficient.

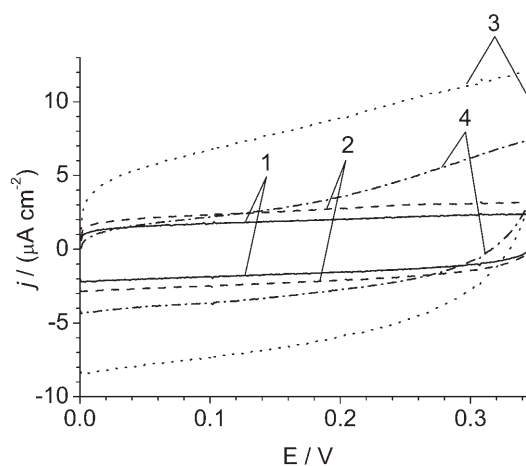


Fig. 5. Comparison of the cyclic voltammograms in 0.1 M Na_2SO_4 . Curve 1 (solid line) was recorded at a 20 nm TiN electrode, curve 2 (dashed line) at a 100 nm TiN electrode, curve 3 (dotted line) at a 300 nm TiN electrode and curve 4 (dash-dotted line) at a gold thin film electrode. $\nu = 50 \text{ mV s}^{-1}$.

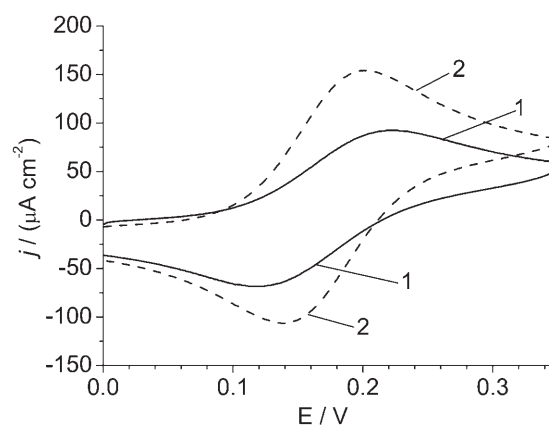


Fig. 6. Cyclic voltammograms of 1 mM ferrocenemethanol in 0.1 M Na_2SO_4 solution. Curve 1 at 300 nm TiN (solid line), curve 2 at gold (dashed line). $\nu = 50 \text{ mV s}^{-1}$.

3.3. SECM Investigation of Electron Transfer Kinetics

The kinetics of the electron transfer were studied using SECM approach curves in the feedback mode. This offers the advantage, that a very low total current is passing through the sample. If the sample is externally polarized, resistive effects inside the electrode material are less important than for instance in cyclic voltammetry. The

Table 1. Negative and positive potential windows of the TiN electrode in different electrolytes.

Layer thickness (nm)	0.05 M H_2SO_4		0.1 M phosphate buffer		0.1 M NaOH	
	negative limit (V)	positive limit (V)	negative limit (V)	positive limit (V)	negative limit (V)	positive limit (V)
20	-0.24	0.86	-0.31	0.60	-0.35	0.43
100	-0.23	0.87	-0.30	0.60	-0.26	0.43
300	-0.23	0.94	-0.32	0.66	-0.37	0.51

instruments records i_T as a function of the vertical position z of the UME (increasing when approaching the surface). The obtained curves were first normalized.

$$I_T' = i_T(L)/i_{T,\infty} \quad (1)$$

$$L = (z_{\text{surface}} - z)/r_T = (z_{\text{touch}} + d_0 - z)/r_T \quad (2)$$

The normalized current I_T' is the distance-dependent steady-state current i_T normalized by the experimental current $i_{T,\infty}$ recorded far away ($>20 r_T$) from the sample surface. The vertical coordinate z is converted to a normalized distance L using the experimentally determined coordinate z_{touch} at which a mechanical touch between the insulating glass sheath of the UME and the surface occurred. At this point the active electrode area has a distance d_0 to the sample surface. This value and the exact r_T were determined by fitting to Equation 4 an experimental approach curve towards a glass substrate with the same UME and the same UME mounting. We found this procedure necessary for high accuracy because otherwise several sets of z_{touch} and normalized rate constants κ could reasonably describe the experimental approach curve in the limited L interval for which an analytical approximation is available.

The experimental approach curve was fitted to the expression derived for approach curves towards samples with finite kinetics at the sample and diffusion-limited current at the UME [42].

$$I_T(L) = \frac{i_T(L)}{4nFD r_T c^*} = \left[I_T^{\text{ins}}(L) + I_S(L) \left(1 - \frac{I_T^{\text{ins}}(L)}{I_T^{\text{cond}}(L)} \right) \right] \quad (3)$$

The contributions to this current I_T^{ins} , I_S and I_T^{cond} were obtained from different approximations taking into account the slightly different normalizations that were used (either the experimental $i_{T,\infty}$ or the analytical expression for the current at a microdisk embedded in an infinitely large insulating sheath ($4nFD r_T c^*$; n : number of transferred electrons per molecule, F : Faraday constant, D : diffusion coefficient of Fc, c^* : bulk concentration of Fc [43]). The contribution for the normalized current for an insulator I_T^{ins} was taken from [44] for $RG = 10.2$. Since this paper gives analytical approximations of the current with respect to the experimentally observed $i_{T,\infty}$ (instead of $4nFD r_T c^*$), a small correction was applied. The factor $i_{T,\infty}/4nFD r_T c^*$ can be taken from [45] and [46].

$$I_T^{\text{ins}}(L) = \frac{i_T^{\text{ins}}(L)}{i_{T,\infty}(RG) \cdot \frac{4nFD r_T c^*}{i_{T,\infty}(RG)}} = \left[\frac{1}{0.42676 + \frac{1.46081}{L} + 0.56874 \cdot \exp\left(\frac{-2.28548}{L}\right)} \right] \cdot 1.019 \quad (4)$$

The contribution I_T^{cond} was taken from [44] for $RG = 10.2$ and corrected for normalizations to $4nFD r_T c^*$.

$$I_T^{\text{cond}}(L) = \frac{i_T^{\text{cond}}(L)}{i_{T,\infty}(RG) \cdot \frac{4nFD r_T c^*}{i_{T,\infty}(RG)}} = \left[0.72637 + \frac{0.76651}{L} + 0.206015 \cdot \exp\left(\frac{-1.41332}{L}\right) \right] \cdot 1.019 \quad (5)$$

The normalized substrate current $I_S = i_S/4nFD r_T c^*$ is the normalized current equivalent at the sample. It can be estimated for $RG = 10$ and $0.1 < L < 1.6$ by the analytical approximation Equation 6 [42].

$$I_S(L, \kappa) = \frac{0.78377}{L \cdot \left(1 + \frac{1}{\kappa L}\right)} + \frac{0.68 + 0.3315 \cdot \exp\left(\frac{-1.0672}{L}\right)}{1 + \left(\frac{11}{110 - 40L}\right)} \quad (6)$$

The calculated current $I_T(L)$ (normalized to $4nFD r_T c^*$) can be compared to the normalized experimental current $I_T'(L)$ (normalized by the experimental $i_{T,\infty}$)

$$I_T'(L) = \frac{i_T(L)}{i_{T,\infty}(RG)} = I_T(L) \cdot \frac{4nFD r_T c^*}{i_{T,\infty}(RG)} = \left[I_T^{\text{ins}}(L) + I_S(L) \cdot \left(1 - \frac{I_T^{\text{ins}}(L)}{I_T^{\text{cond}}(L)} \right) \right] \cdot 1.019 \quad (7)$$

By variation of the value κ in Equation 6 and $i_{T,\infty}$ in Equation 1, the calculated values for $I_T'(L)$ from Equation 7 may be brought into agreement with the experimental curve. From κ , an effective heterogeneous first order rate constant k_{eff} can be derived from Equation 8 [42]

$$k_{\text{eff}} = \kappa D / r_T \quad (8)$$

Examples of fitted experimental approach curves are given in Figure 7 for native and UV-ozone-treated TiN of 100 nm thickness. It shows already qualitatively clear differences in the rate constant with the applied sample potential and pretreatment. For calculation of k_{eff} , $D_O = D_R = D$ was assumed. The value $D = 6 \times 10^{-6} \text{ cm}^2 \text{ s}^{-1}$ was obtained from chronoamperometric measurements of ferrocenemethanol. With knowledge of k_{eff} for every E_s , an apparent heterogeneous standard rate constant k° can be extracted using the Butler–Volmer equation (Eq. 9) for sufficiently high overvoltages.

$$\ln k_{\text{eff}} = \ln k^\circ - \alpha(nF/RT)(E_s - E^\circ) \quad (9)$$

where α is the transfer coefficient, R the gas constant, and T the temperature. As an example the plot for three different

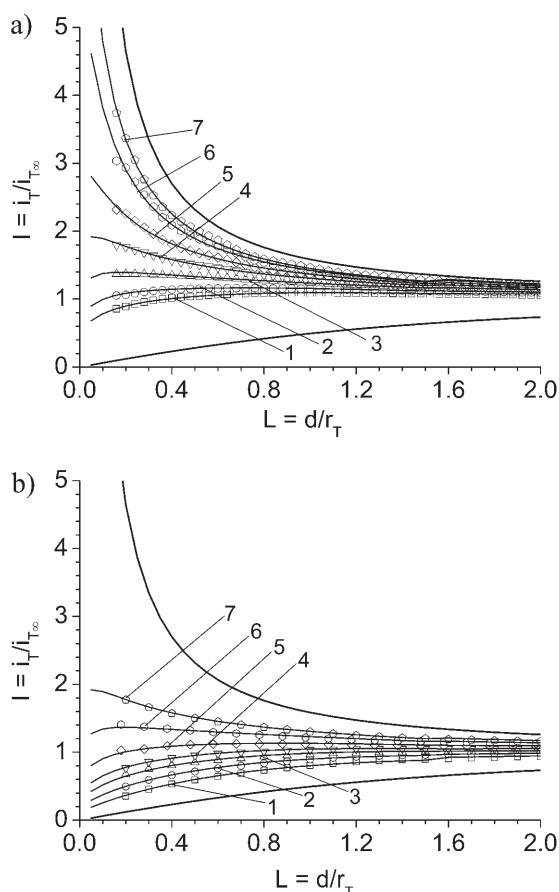


Fig. 7. Normalized approach curves towards a 100 nm thick TiN sample before (a) and after (b) ozone treatment. The experimental curves (open symbols) at different substrate potentials E_S were fitted with the following normalized rate constants κ . a) (1) $E_S = 150$ mV, $\kappa = 0.66$, (2) $E_S = 100$ mV, $\kappa = 0.91$, (3) $E_S = 50$ mV, $\kappa = 1.42$, (4) $E_S = 0$ mV, $\kappa = 2.25$, (5) $E_S = -50$ mV, $\kappa = 3.65$, (6) $E_S = -100$ mV, $\kappa = 7.27$, (7) $E_S = -150$ mV, $\kappa = 12$. b) (1) $E_S = 150$ mV, $\kappa = 0.15$, (2) $E_S = 100$ mV, $\kappa = 0.25$, (3) $E_S = 50$ mV, $\kappa = 0.385$, (4) $E_S = 0$ mV, $\kappa = 0.52$, (5) $E_S = -50$ mV, $\kappa = 0.8$, (6) $E_S = -100$ mV, $\kappa = 1.37$, (7) $E_S = -150$ mV, $\kappa = 2.25$. Thick lines show the expected behavior for hindered diffusion ($\kappa = 0$) and diffusion-controlled Fc recycling ($\kappa = \infty$).

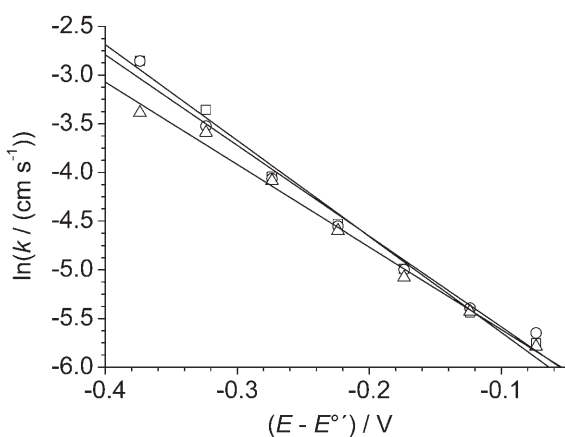


Fig. 8. Plot of the effective rate constants obtained from approach curves towards a 100 nm TiN sample in (Δ) 1.0 mM, (\bullet) 2.0 mM and (\square) 3.0 mM ferrocenemethanol solutions.

Table 2. Apparent standard rate constants of the Fc/Fc⁺ couple as a function of the TiN layer thickness for native TiN and UV/ozone-treated TiN.

TiN thickness (nm)	k° (10^{-3} cm s ⁻¹) [a]	
	native TiN	UV/ozone-treated TiN
20	0.97	0.98
100	1.5	0.84
300	2.2	1.9

[a] averaged from three different Fc concentrations.

Fc concentrations at a 100 nm thick native TiN sample is shown in Figure 8. The mean of the apparent standard rate constants obtained from similar plots for TiN layers of 20 nm, 100 nm and 300 nm thickness before and after UV/ozone treatment are given in Table 2. The UV/ozone treatment turned out to be not beneficial for the redox kinetics although XPS had shown an effective removal of organic contamination. Most likely, the thin surface layer of TiO₂ on the TiN samples was enlarged and decreased the electron transfer kinetics even more effectively than the organic contamination layer present after storage in air. There is a clear effect of the thickness of the TiN layers on the apparent electron transfer kinetics. This could be a consequence of the increased surface area for thicker TiN layers (Fig. 1).

4. Conclusions

Thin films of titanium nitride were tested for their direct use as electrodes in electroanalytical measurements, i.e. without previous coating by another metal. These electrodes offer advantages by their mechanical hardness and relative inertness to organic contaminations during prolonged storage. This can be particularly interesting for microstructured devices. They can be produced in well adhering thin layers by an established technology that opens possibilities for mass-producing nanometer-sized electrodes. The potential range in aqueous solutions is large enough for many compounds used for instance in electrochemical detections of immunoassays. The electron transfer kinetics of redox couples that are considered reversible at conventional noble metal electrodes is clearly slower at TiN, however, still in a useful range if some overvoltage can be applied without causing interference problems. This situation might be encountered in read-out procedure for electrochemical immunoassays or DNA assays. The double layer capacity is higher than at gold electrodes. It can to some extent be tuned by controlling the crystal morphology of the TiN films and the film thickness. Nevertheless, the charging currents suggest that TiN electrodes may be better applied in amperometric (at constant potential) than in voltammetric detection schemes.

5. Acknowledgements

This work has been supported by the University of Oldenburg. We would like to thank Achim Kittel, University of Oldenburg, Department of Physics for the four-point resistance measurements. We gratefully thank Sascha E. Pust for the help in the SFM measurement.

6. References

- [1] J. Crummenauer, H. R. Stock, P. Mayr, *Mater. Manuf. Processes* **1995**, *10*, 1267.
- [2] L. A. Cyster, D. M. Grant, K. G. Parker, T. L. Parker, *Biomol. Eng.* **2002**, *19*, 171.
- [3] K. Holmberg, A. Matthews, in *Wear Materials, Mechanisms and Practice, Tribology of Engineered Surfaces* (Eds: G. W. Stachowiak), Wiley, Chichester **2004**.
- [4] L. E. Toth, *Transition Metal Carbides and Nitrides*, Academic Press, New York **1971**.
- [5] N. J. Archer, *Thin Solid Films* **1981**, *80*, 221.
- [6] R. Roth, J. Schubert, M. Martin, E. Fromm, *Thin Solid Films* **1995**, *270*, 320.
- [7] J. E. Sundgren, *Thin Solid Films* **1985**, *128*, 21.
- [8] Z. Y. Chen, A. W. Castleman, Jr., *J. Chem. Phys.* **1993**, *98*, 231.
- [9] S. A. Catledge, M. Fries, Y. K. Vohra, *Nanostructured Surface Modifications for Biomedical Implants*, American Scientific Publishers, Stevenson Ranch, California **2004**.
- [10] M. R. L. Glew, A. Vollmer, S. L. M. Schroeder, Z. H. Barber, *J. Phys. D: Appl. Phys.* **2002**, *35*, 2643.
- [11] M. Guemaz, G. Moraitis, A. Mosser, M. A. Khan, J. C. Parlebas, *J. Phys.: Condens. Matter* **1997**, *9*, 8453.
- [12] H. Q. Lou, N. Axen, R. E. Somekh, I. M. Hutchings, *Surf. Coat. Technol.* **1997**, *90*, 123.
- [13] B. Rauschenbach, J. W. Gerlach, *Cryst. Res. Technol.* **2000**, *35*, 675.
- [14] F. Vaz, J. Ferreira, E. Ribeiro, L. Rebouta, S. Lanceros-Mendez, J. A. Mendes, E. Alves, P. Goudeau, J. P. Riviere, F. Ribeiro, I. Moutinho, K. Pischow, J. de Rijk, *Surf. Coat. Technol.* **2005**, *191*, 317.
- [15] K. Yokota, K. Nakamura, T. Kasuya, K. Mukai, M. Ohnishi, *J. Phys. D: Appl. Phys.* **2004**, *37*, 1095.
- [16] A. J. Dowling, M. K. Ghantasala, J. P. Hayes, E. C. Harvey, E. D. Doyle, *Smart Mater. Struct.* **2002**, *11*, 715.
- [17] M. Black, J. Cooper, P. McGinn, *Meas. Sci. Technol.* **2005**, *16*, 174.
- [18] L. A. Cyster, K. G. Parker, T. L. Parker, D. M. Grant, *Biomaterials* **2003**, *25*, 97.
- [19] L. A. Rocha, E. Ariza, J. Ferreira, F. Vaz, E. Ribeiro, L. Rebouta, E. Alves, A. R. Ramos, P. Goudeau, J. P. Riviere, *Surf. Coat. Technol.* **2004**, *180–181*, 158.
- [20] N. C. Saha, H. G. Tompkins, *J. Appl. Phys.* **1992**, *72*, 3072.
- [21] H. G. Tompkins, *J. Appl. Phys.* **1991**, *70*, 3876.
- [22] H. G. Tompkins, *J. Appl. Phys.* **1992**, *71*, 980.
- [23] Y. Wang, H. Yuan, X. Lu, Z. Zhou, D. Xiao, *Electroanalysis* **2006**, *18*, 1493.
- [24] T. Nakayama, H. Wake, K. Ozawa, H. Kodama, N. Nakamura, T. Matsunaga, *Environ. Sci. Technol.* **1998**, *32*, 798.
- [25] L. A. Cyster, K. G. Parker, T. L. Parker, D. M. Grant, *J. Biomed. Mater. Res. Part A* **2003**, *67A*, 138.
- [26] G. Sanchez, E. Dalchiele, A. Bologna Alles, *J. Mater. Sci.* **2006**, *41*, 3241.
- [27] K. Aoki, M. Morita, O. Niwa, H. Tabei, *J. Electroanal. Chem.* **1988**, *256*, 269.
- [28] M. Paeschke, U. Wollenberger, C. Köhler, T. Lisec, U. Schnakenberg, R. Hintsche, *Anal. Chim. Acta* **1995**, *305*, 126.
- [29] R. M. Ranade, S. S. Ang, W. D. Brown, *J. Electrochem. Soc.* **1993**, *140*, 3676.
- [30] F. T. Aldridge, *J. Electrochem. Soc.* **1995**, *142*, 1563.
- [31] A. Efremov, V. Svetsov, C.-I. Kim, *Proc. SPIE* **2003**, *5401*, 64.
- [32] L. Jiao, H. Gao, G. Zhang, G. Xie, X. Zhou, Y. Zhang, Y. Zhang, B. Gao, G. Luo, Z. Wu, T. Zhu, J. Zhang, Z. Liu, S. Mu, H. Yang, C. Gu, *Nanotechnology* **2005**, *16*, 2779.
- [33] S. A. Campbell, *The Science and Engineering of Micro-electronic Fabrication*, Oxford University Press, New York **2001**.
- [34] S. A. G. Evans, J. G. Terry, N. O. V. Plank, A. J. Walton, L. M. Keane, C. J. Campbell, P. Ghazal, J. S. Beattie, T.-J. Su, J. Crain, A. R. Mount, *Electrochem. Commun.* **2005**, *7*, 125.
- [35] J. Baumann, *Herstellung, Charakterisierung und Bewertung von leitfähigen Diffusionsbarrieren auf Basis von Ta, Ti und W für die Kupfermetallisierung von Siliciumschaltkreisen*, Shaker Verlag, Herzogenrath, **2004**.
- [36] R. Hesse, P. Streubel, R. Szargan, *Surf. Interface Anal.* **2005**, *37*, 589.
- [37] C. Kranz, M. Ludwig, H. E. Gaub, W. Schuhmann, *Adv. Mater.* **1995**, *7*, 38.
- [38] H. Höchst, R. D. Bringans, P. Steiner, T. Wolf, *Phys. Rev. B: Condens. Matter Mater. Phys.* **1982**, *25*, 7183.
- [39] J. Guillot, J.-M. Chappé, O. Heintz, N. Martin, L. Imhoff, J. Takadoum, *Acta Materialia* **2006**, *54*, 3067.
- [40] S. Badrinarayanan, S. Sinha, A. B. Mandale, *J. Electron Spectrosc. Relat. Phenom.* **1989**, *49*, 303.
- [41] R. S. Nicholson, *Anal. Chem.* **1965**, *37*, 1351.
- [42] C. Wei, A. J. Bard, M. V. Mirkin, *J. Phys. Chem.* **1995**, *99*, 16033.
- [43] Y. Saito, *Rev. Polarogr.* **1968**, *15*, 177.
- [44] J. L. Amphlett, G. Denuault, *J. Phys. Chem. B* **1998**, *102*, 9946.
- [45] C. G. Zoski, M. V. Mirkin, *Anal. Chem.* **2002**, *74*, 1986.
- [46] G. Denuault, personal communication.